



Photoelectrochemical Properties of MOF Induced Surface Modified TiO₂ Photoelectrode

Journal:	<i>Nanoscale</i>
Manuscript ID	NR-ART-08-2018-006471.R1
Article Type:	Paper
Date Submitted by the Author:	25-Sep-2018
Complete List of Authors:	Feng, Pingyun; University of California, Department of Chemistry Jiao, Wei; Fudan University, Department of Chemistry Zhu, Jiaying; Fudan University, Department of Chemistry Ling, Yun; Fudan University, Chemistry Deng, Mingli; Fudan University, Chemistry Zhou, Yaming; Fudan University, Chemistry Department





Journal Name

ARTICLE

Photoelectrochemical Properties of MOF Induced Surface Modified TiO₂ Photoelectrode

Wei Jiao,^{a, b} Jiaxing Zhu,^a Yun Ling,^b Mingli Deng,^a Yaming Zhou^{*a} and Pingyun Feng^{*b}

Received 00th January 20xx,
Accepted 00th January 20xx

DOI: 10.1039/x0xx00000x

www.rsc.org/

Heteroatom doping and surface modification with other oxides are both important strategies to improve the photoelectrochemical (PEC) activities of TiO₂ photoelectrode. However, it is difficult to simultaneously combine the two strategies together in one synthesis process. Here, a simple one-pot synthetic method is developed to simultaneously modify TiO₂ photoelectrode surface by N-doping and surface modification with In₂O₃ and NiO. This method is achieved by growing MOF with N-containing organic ligand and In and Ni salts as metal precursors onto TiO₂ surface, followed by heat treatment at 600 °C. The roles of heteroatom doping and oxides modification are proposed as (i) N-doping extends the absorption edge of the TiO₂ to longer wavelength region and enhances the visible light absorption. (ii) N-doping together with the passivation of TiO₂ surface trap states by oxides modification increase the donor density in the TiO₂. (iii) Generated suitable interfaces on the surface of TiO₂ that facilitate photogenerated charge separation and transfer. In comparison with the pristine TiO₂ photoelectrode, the metal oxides and heteroatom modified TiO₂ photoelectrode exhibits superior photoelectrochemical performance under both simulated sunlight and visible light illumination. Suitable substrate of the electrode, appropriate size of the synthesized MOF precursors, choice of ligands and metal ions are all important factors for this strategy.

Introduction

Photoelectrochemical water splitting is a promising method to convert solar energy into chemical energy, which is critical for sustainable and clean energy supply.^{1, 2} Among many photocatalysts, TiO₂ based photoelectrode has attracted much interest because of its suitable band structure, stability, low cost and low toxicity.³⁻⁶ Many attempts were made to improve the reactivity of the TiO₂ photoelectrode, such as doping,⁷⁻⁹ co-catalyst,¹⁰⁻¹² heterostructure¹³ and morphology control.¹⁴⁻¹⁶ However, due to its low electron and hole separation efficiency and low visible light absorption, it remains a challenge for TiO₂ to be applied in photoelectrochemical water splitting.

In comparison with pure TiO₂, surface modified TiO₂ showed improved photoelectrochemical activities. For example: Li et al. treated TiO₂ nanowires with hydrogen to form oxygen vacancies on the surface of TiO₂. With the increase of the donor density, these oxygen vacancies enhanced the photocurrent of TiO₂

photoelectrode.¹⁷ Mullins et al. synthesized N-modified TiO₂ nanowires with cobalt as a co-catalyst. By doping and co-catalyst modification, the photoelectrochemical performance was enhanced both in ultraviolet and visible light region.¹⁸ Lin et al. deposited Cu₂O on the surface of TiO₂ nanotube arrays to form the p-n junction. As a result, the separation of photoinduced holes and electrons was improved and the Cu₂O/TiO₂ hybrid photoelectrode exhibited superior performance.¹⁹ So far, great progress has been made in TiO₂ surface modification. However, modifying TiO₂ surface with multiple heteroatom and metal oxides simultaneously is still a challenge task for specific application.

Metal organic frameworks (MOFs) are a type of porous materials with unique atomic ordering.^{20, 21} MOFs can be constructed with different organic ligands and metal ions. Because of their diverse chemical compositions and tunable structures, these MOFs are considered to be promising materials for many applications, including CO₂ capture, catalysis and energy conversion and storage. The flexible chemical composition of MOFs also makes them ideal precursors for modifying the surface of TiO₂ photoelectrode with complex composition and structure for different functionalities.

From the synthetic point view, with MOF as a precursor to induce surface modification of TiO₂ for improving the photoelectrochemical properties, two key strategies need to be considered. One is the synthesis of a suitable TiO₂ substrate for hosting MOF material; The second one is to deposit MOFs precursors with proper metallic and

^a Shanghai Key Laboratory of Molecular Catalysis and Innovative Materials, Department of Chemistry, Fudan University, Shanghai 200433, China E-mail: ymzhou@fudan.edu.cn

^b Department of Chemistry, University of California, Riverside, CA 92521, USA E-mail: pyfeng@ucr.edu

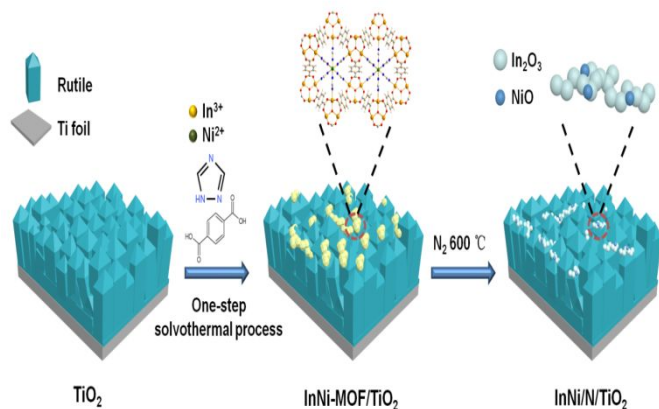
Electronic Supplementary Information (ESI) available: SEM images of the pristine TiO₂ electrode and the InNi/N/TiO₂ electrode with 12 h synthesis time, Transient photocurrents of the pristine TiO₂ and InNi/N/TiO₂ photoelectrodes with different synthesis time and the InNi/N/TiO₂ annealed with different temperatures. See DOI: 10.1039/x0xx00000x

nonmetallic elements on the surface. With the above consideration, firstly, we synthesized a Ti^{3+} doped TiO_2 substrate.⁶ The existence of Ti^{3+} could lead to more surface defect and this may enhance the interaction of the ligands in the MOF precursor solution and TiO_2 surface. Secondly, we choose to deposit a MOF with In and Ni metal ions, and 1,2,4-triazolate as the ligand which contained N atom.²² Our strategy is to construct Ti^{3+} and N co-doped TiO_2 combined with the deposition of specific metal oxides on the surface to enhance the light absorption and to construct the suitable interfaces ($\text{TiO}_2/\text{In}_2\text{O}_3/\text{NiO}$) to promote the separation of photogenerated electron-hole pairs for the TiO_2 photoelectrode.

With the above strategies, metal oxides and heteroatom modified TiO_2 based photoelectrode named as $\text{InNi}/\text{N}/\text{TiO}_2$ was successfully synthesized. The loading status of the MOF precursors could be controlled by varying the synthesis conditions. The modification derived with MOF of different chemical compositions helps in tuning the surface electronic structure, properties of charges separation and transfer and photoelectrochemical activities of TiO_2 . Compared to the pristine TiO_2 photoelectrode, the photoelectrochemical performance of $\text{InNi}/\text{N}/\text{TiO}_2$ photoelectrode was enhanced obviously.

Results and discussion

The synthetic process for making $\text{InNi}/\text{N}/\text{TiO}_2$ is illustrated in scheme 1. Firstly, the Ti^{3+} doped rutile TiO_2 electrode was synthesized using a modified procedure from our previous work.⁶ Then, the TiO_2 electrode was immersed into the solution containing MOF precursors (In^{3+} , Ni^{2+} , 1,2,4-triazol and terephthalic acid). With a subsequent solvothermal treatment, the InNi-MOF grew on the surface of TiO_2 ($\text{InNi-MOF}/\text{TiO}_2$). After a thermal treatment at $600\text{ }^\circ\text{C}$ in N_2 atmosphere, InNi-MOF was decomposed and the In_2O_3 and NiO modified rutile TiO_2 electrode with co-doping of N and Ti^{3+} was obtained.



Scheme 1. Schematic illustration of the one-step synthesis of a InNi-MOF modified rutile TiO_2 and its derived In_2O_3 , NiO and N modified rutile TiO_2 .

The X-ray diffraction (XRD) patterns of TiO_2 electrode, $\text{InNi-MOF}/\text{TiO}_2$ electrode and $\text{InNi}/\text{N}/\text{TiO}_2$ electrode are shown in Fig. 1.

The as-prepared TiO_2 on the surface of the Ti foil is rutile TiO_2 . The XRD pattern of $\text{InNi-MOF}/\text{TiO}_2$ is shown in Fig. 1a. The diffraction peak at 8.8° and 12.8° can be indexed to (00-2) and (-120) facets of InNi-MOF , which confirm the formation of InNi-MOF on the surface of TiO_2 . In comparison, the XRD (Fig. 1b) of the electrode annealed at $600\text{ }^\circ\text{C}$ ($\text{InNi}/\text{N}/\text{TiO}_2$) shows no other phases except for the rutile TiO_2 and Ti metal. This is because the small amount of oxides derived from the pyrolysis of the InNi-MOFs is below the measurable limit of XRD characterization.

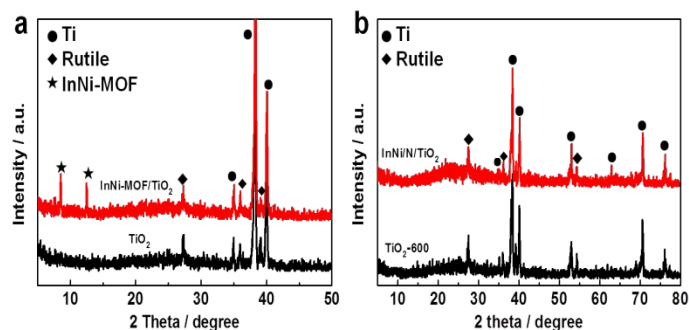


Fig. 1 XRD patterns of (a) TiO_2 electrode and $\text{InNi-MOF}/\text{TiO}_2$, (b) $\text{InNi}/\text{N}/\text{TiO}_2$ and TiO_2 electrode annealed at $600\text{ }^\circ\text{C}$.

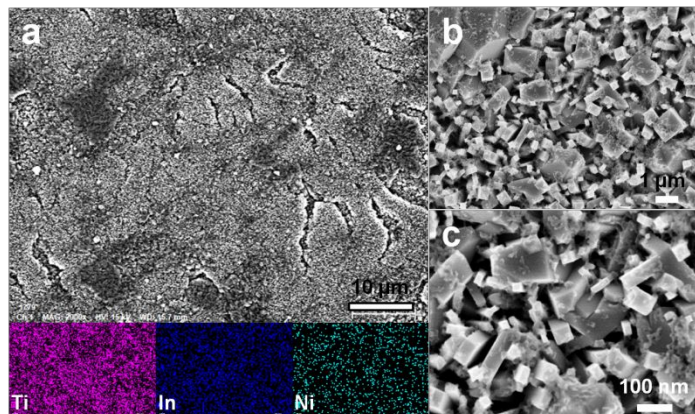


Fig. 2 (a) Low magnification SEM image and responding elemental mapping, (b, c) high magnification SEM images of $\text{InNi-MOF}/\text{TiO}_2$.

The scanning electron microscopy (SEM) images of TiO_2 electrode are shown in Fig. S1, which show most of the rutile TiO_2 crystals grown on the Ti foil are rectangular pyramids with four {110} facets in the middle parts and four {111} facets on the top of the crystals.²³ The surfaces of the rectangular pyramids are very smooth without any other clusters or particles on them. The corresponding cross-sectional views of TiO_2 electrode in Fig. S1b and d show the rectangular pyramid morphology of TiO_2 and the interface between the TiO_2 and Ti foil substrate clearly. The thickness of TiO_2 layer is about $2\text{ }\mu\text{m}$. The SEM image and corresponding elemental mapping of $\text{InNi-MOF}/\text{TiO}_2$ electrode in Fig. 2a show homogeneous distribution of Ti, In and Ni, which indicates that the InNi-MOF particles are distributed uniformly on the TiO_2 electrode. As shown in Fig. 2b and c, the InNi-MOF nanoparticles with particle sizes from 20 nm to 100 nm were deposited on

the facet of the TiO_2 after the growth process of InNi-MOF. MOFs crystals usually have large size of about several micrometers, which is disadvantageous for the light absorption of TiO_2 and the transportation of the carriers. By reducing the precursor concentration and reaction time in the MOF synthesis, the InNi-MOF particles grown on the surface of TiO_2 have much small size. These small sizes could be helpful in the construction of suitable heterostructures for improving the performance of electrode. By annealing at 600°C under N_2 flow, the In_2O_3 and NiO nano-particles are formed on the surface of TiO_2 as shown from the SEM images in Fig. 3. The SEM image and corresponding elemental mapping of InNi/N/ TiO_2 electrode in Fig. 3a also show homogeneous signals for Ti, In and Ni, which demonstrates the uniform distribution of In_2O_3 and NiO on the surface of TiO_2 after heat treatment. In Fig. 3b and e, it is shown that the In_2O_3 and NiO decomposed from the InNi-MOF are all nano-particles with smaller particle sizes than the InNi-MOF. The transmission electron microscopy (TEM) images of nano-particles grown on the TiO_2 were shown in Fig. 3c and f. The sizes of the particles are about 15 nm to 40 nm as shown in Fig. 3c. The high-resolution TEM image (the inner part of the white box in Fig. 3c) in Fig. 3e confirms that the particles are consist of two kinds of oxides: In_2O_3 with a size of around 20 nm and NiO with a size of around 5 nm. The distinct lattice spacings of 0.29 nm and 0.21 nm observed in the two particles corresponds to In_2O_3 (222) and NiO (200), respectively. The TEM images of In_2O_3 , NiO and TiO_2 are shown in Fig. 3d and g. It is clearly indicated that the In_2O_3 and NiO particles are grown on the surface of TiO_2 and there is a good connection between the interface of TiO_2 and In_2O_3 or NiO particles for the designed in-situ growth process, which is beneficial for the transfer of carriers.

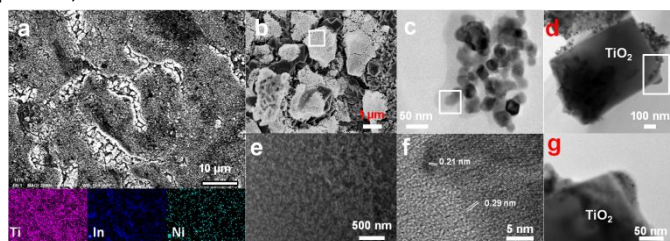


Fig. 3 (a) Low magnification SEM image and responding elemental mapping, (b, e) high magnification SEM images of InNi/N/ TiO_2 , (c) TEM image and (f) HRTEM image of In_2O_3 and NiO particles, (d, g) TEM images of InNi/N/ TiO_2 .

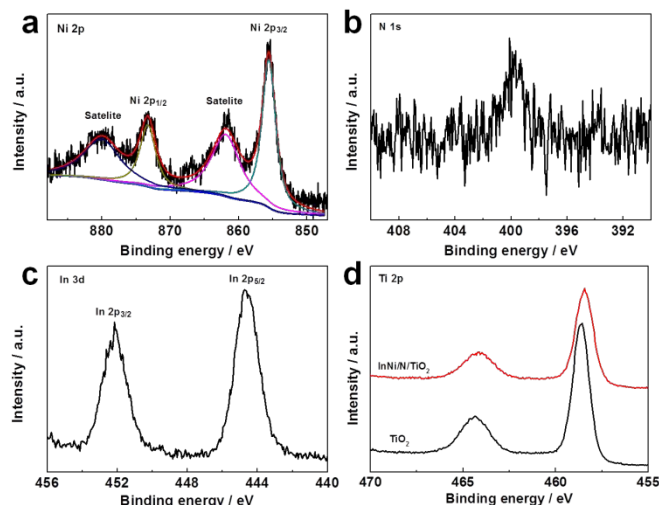


Fig. 4 XPS spectra of (a) Ni 2p, (b) N 1s, (c) In 3d in InNi/N/ TiO_2 and (d) Ti 2p in the InNi/N/ TiO_2 and the pristine TiO_2 .

The surface chemical state of the InNi/N/ TiO_2 is determined by the X-ray photoelectron spectroscopy (XPS) as shown in Fig. 4. High resolution XPS spectrum of the Ni 2p in Fig. 4a reveals that the two peaks at 855.5 and 873.5 eV originate from Ni $2p_{3/2}$ and $2p_{1/2}$ of NiO on the surface of TiO_2 ,^{24, 25} respectively. The binding energies of 861.5 and 879.9 eV are identified as the satellite peaks of Ni $2p_{3/2}$ and $2p_{1/2}$ of NiO. As shown in Fig. 4c, the binding energies at 444.6 and 452.1 eV originate from the In $2p_{5/2}$ and $2p_{3/2}$ in In_2O_3 ,²⁶ respectively. The N 1s signal detected in Fig. 4b confirms the existence of N species in InNi/N/ TiO_2 . The binding energy ranging from 401 to 398 eV suggests the interstitial incorporated of N in TiO_2 and minor molecularly chemisorbed N_2 species exist.^{27, 28} The atomic percentages of nitrogen, indium and nickel in InNi/N/ TiO_2 are 1 %, 3.5 % and 1.2 %, respectively.

In comparison to the UV-visible absorption spectra of pristine TiO_2 , the InNi/N/ TiO_2 did show a red shift as shown in Fig. 5a. In addition, the light absorption in the visible light region (450 nm to 800 nm) is also enhanced due to the existence of In_2O_3 and NiO on the surface of TiO_2 compared to the pristine TiO_2 .^{29, 30} It is worth noting that the similar absorption bands of InNi/N/ TiO_2 and TiO_2 from 420 nm to 800 nm, which are attributed to Ti^{3+} ,³¹ confirm the existence of Ti^{3+} in InNi/N/ TiO_2 , because of the protection of nitrogen atmosphere in the heat treatment process. According to the plot of transformed Kubelka-Munk function in Fig. 5b, the bandgap of InNi/N/ TiO_2 is reduced to 2.88 eV, compared to the bandgap of 3.03 eV of the pristine TiO_2 . By heteroatom doping and surface modification with different oxides, the surface electronic structure of the InNi/N/ TiO_2 was adjusted successfully.

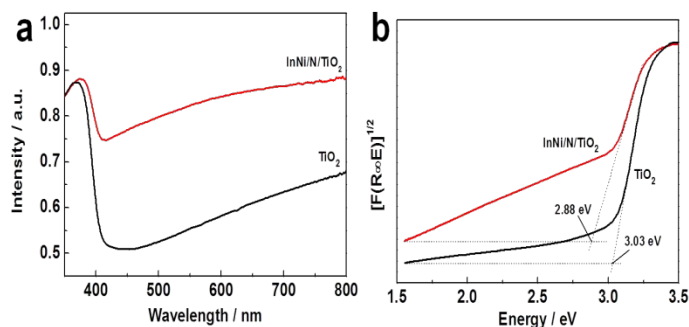


Fig. 5 (a) UV-visible absorption spectra and (b) plot of transformed Kubelka-Munk function for InNi/N/TiO₂ and pristine TiO₂ photoelectrode.

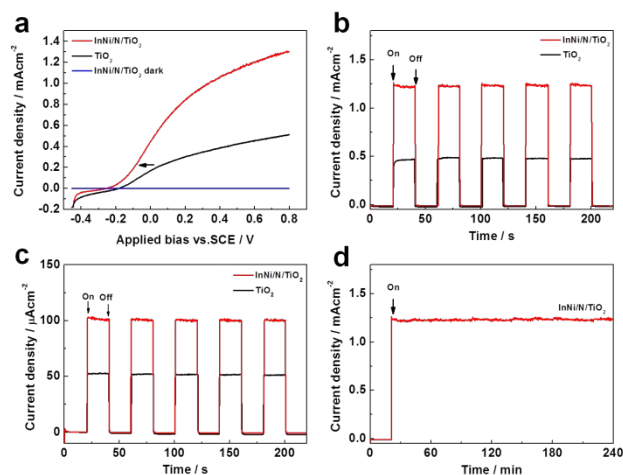


Fig. 6 (a) Linear sweeps voltammograms for the InNi/N/TiO₂ and the pristine TiO₂ photoelectrodes at a scan rate of 10 mV/s under 100 mW/cm² simulated sunlight illumination, (b) transient photocurrents for InNi/N/TiO₂ and pristine TiO₂ photoelectrodes at 0.6 V vs SCE under 100 mW/cm² simulated sunlight illumination, (c) transient photocurrents for the InNi/N/TiO₂ and the pristine TiO₂ photoelectrodes at 0.6 V vs SCE under visible light illumination (>400 nm), (d) time-dependant photocurrent for the InNi/N/TiO₂ photoelectrode at 0.6 V vs SCE under 100 mW/cm² simulated sunlight illumination.

The photoelectrochemical activities of the InNi/N/TiO₂ photoelectrode and pristine TiO₂ photoelectrode were tested in a standard three-electrode electrochemical cell, using Pt foil as the counter electrode, a saturated calomel electrode (SCE) as the reference electrode and 0.5 M Na₂SO₄ (pH=6.3) as the electrolyte. The linear sweeps were firstly measured under 100 mW/cm² simulated sunlight illumination from a 150 W Xenon lamp coupled with a AM 1.5G filter (see details in the experimental section). As shown in Fig. 6a, a obviously enhanced photocurrent was observed for the InNi/N/TiO₂. The photocurrent density of the InNi/N/TiO₂ photoelectrode is 1.28 mA/cm² at 0.6 V vs SCE, which is 2.7 times higher than that of the pristine TiO₂ photoelectrode. Moreover,

compared with the pristine TiO₂ photoelectrode, the onset potential of the InNi/N/TiO₂ photoelectrode is decreased by about 73 mV, which could be contributed from the surface modification of the oxides.³² The transient photocurrents of InNi/N/TiO₂ photoelectrode and pristine TiO₂ photoelectrode at 0.6 V vs SCE are shown in Fig. 6b, the current densities for InNi/N/TiO₂ photoelectrode and pristine TiO₂ photoelectrode are 1.29 mA/cm² and 0.45 mA/cm², which match well with the data of linear sweep voltammograms. More importantly, the InNi/N/TiO₂ photoelectrode shows better performance under visible light irradiation (> 400 nm, details in the experimental section) than that of the pristine TiO₂ as shown in Fig. 6c. Because the co-doping of N and Ti³⁺ in the TiO₂ induced visible-light absorption, the photocurrent at 0.6 V vs SCE for InNi/N/TiO₂ photoelectrode increases from 52 μA/cm² to 101 μA/cm², comparing with the pristine TiO₂ photoelectrode. In addition, we also measured the time-dependent photocurrent at 0.6 V under 100 mW/cm² simulated sunlight illumination (shown in Fig. 6d), which shows no significant attenuation of the photocurrent in about 4 hours, suggesting the excellent stability of the InNi/N/TiO₂ photoelectrode.

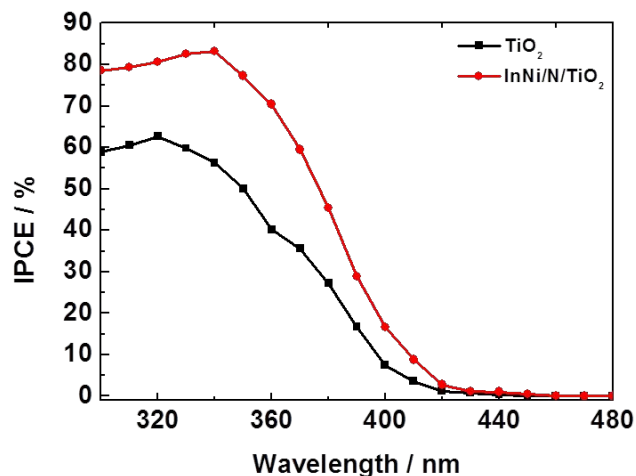


Fig. 7 IPCE spectra of InNi/N/TiO₂ and pristine TiO₂ collected at 0.6 V vs SCE.

Incident-photon-current-conversion efficiency (IPCE) is conducted to compare the conversion efficiency for different photoelectrodes under standard light source irradiation. IPCE can be expressed by the following equation:

$$\text{IPCE} = \frac{1240 \cdot J}{\lambda \cdot E(\lambda)} \times 100 \% \quad (1)$$

Where the *J* is the obtained photocurrent density at a specific incident wavelength, the λ is the wavelength of incident light, and the $E(\lambda)$ is the irradiance at a specific incident wavelength. We measured the IPCE on the InNi/N/TiO₂ photoelectrode and pristine TiO₂ photoelectrode at 0.6 V vs SCE, which are shown in Fig. 7. The maximum IPCE of InNi/N/TiO₂ photoelectrode is 83.2 % at 340 nm, which is about 1.4 times higher than that of pristine TiO₂ photoelectrode. It shows that the InNi/N/TiO₂ photoelectrode exhibits

obviously improved IPCE over UV region. Significantly, the IPCE of InNi/N/TiO₂ photoelectrode from 400 to 420 nm is also much higher than that of pristine TiO₂ photoelectrode. It suggests that modification with N and metal oxides is an efficient method to improve the performance of TiO₂ photoelectrode in both UV and visible region.

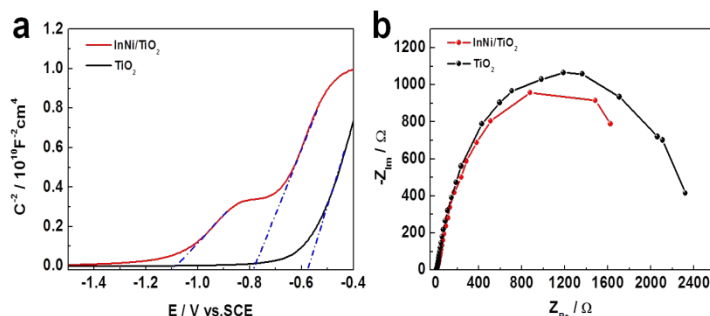


Fig. 8 (a) Mott-Schottky plots for InNi/N/TiO₂ and pristine TiO₂ collected at 0.6 V vs SCE under 100 mW/cm² simulated sunlight illumination, (b) Nyquist plots for InNi/N/TiO₂ and pristine TiO₂ under 100 mW/cm² simulated sunlight illumination.

To further investigate how the surface modification enhanced the charge transfer and separation, the Mott-Schottky plots and electrochemical impedance spectroscopy (EIS) of InNi/N/TiO₂ photoelectrode and pristine TiO₂ photoelectrode were conducted. As shown in Fig. 8a, the Mott-Schottky plots of both InNi/N/TiO₂ and pristine TiO₂ were collected with a bias of 0.6 V vs SCE at 1 KHz under AM 1.5G irradiation (100 mW/cm²). The positive slopes in the plots are consistent with the N-type semiconductor. The Mott-Schottky plots are given by the equation: $1/C^2 = 2(E - E_{fb} - kt/e) / \epsilon \epsilon_0 e N_d$,³³ where the C is the interfacial capacitance, E is the applied bias, k is the Boltzmann constant, the t is the absolute temperature, e is the electronic charge, ϵ is the dielectric constant of the semiconductor and ϵ_0 is the permittivity of free space. The equation can be used to calculate the donor density (N_d) from the E_{fb} and the value of the slope. The InNi/N/TiO₂ photoelectrode shows a smaller slope and more negative E_{fb} compared to these of the pristine TiO₂ photoelectrode, according to the equation above, which indicated an increased donor density in the InNi/N/TiO₂ photoelectrode. The N-doping could enhance the Ti³⁺ states, which is regarded as a kind of donor-type impurity in TiO₂.³⁴⁻³⁶ Besides, deposition of oxides on the surface of TiO₂ could passivate the trap states to prevent from acting as the charge trap centers.³³ For these two reasons, the carrier concentration was increased and thereby the conductivity of the electrode was improved.

It is interesting that the flat band potential (E_{fb}) of InNi/N/TiO₂ photoelectrode shifted to a more negative potential at -0.79 V vs SCE compared to the E_{fb} of pristine TiO₂ at -0.58 V vs SCE. It is probably caused by the deposition of oxides on the surface of TiO₂.³⁵ The negative shift of E_{fb} facilitates the efficiency of charge carriers separation by increasing the degree of band bending to accelerate the migration of electrons and holes to the different directions at the interface.³⁷ The Mott-Schottky plots of InNi/N/TiO₂ photoelectrode exhibits another E_{fb} at -1.1 V vs SCE. It could be related to the

different surface states from the deposited In₂O₃ and NiO or N and Ti³⁺ co-doping on the surface of TiO₂.³⁸⁻⁴⁰

Charge transfer properties of InNi/N/TiO₂ photoelectrode and pristine TiO₂ photoelectrode under illumination were characterized by electrochemical impedance spectroscopy. EIS measurements were carried out with a bias of 0.6 V vs SCE from 0.1 Hz to 10⁵ Hz under AM 1.5G illumination. Fig. 8b displays the Nyquist plots of InNi/N/TiO₂ photoelectrode and pristine TiO₂ photoelectrode respectively. Both InNi/N/TiO₂ photoelectrode and pristine TiO₂ photoelectrode show single capacitive arc. The diameters of two arcs are related to the charge transfer resistance in the charge transfer process.⁴¹ InNi/N/TiO₂ photoelectrode exhibits an arc with a smaller diameter than that of pristine TiO₂ photoelectrode under irradiation suggesting that the InNi/N/TiO₂ photoelectrode is more efficient in photogenerated charges transfer and separation.

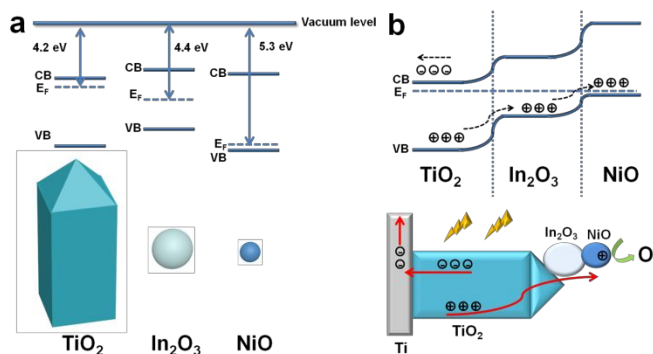


Fig. 9 (a) Band energy diagram of rutile TiO₂, In₂O₃ and NiO before contact and (b) schematic of the InNi/N/TiO₂ photoelectrode showing the promoted transfer of photogenerated electrons and holes from TiO₂ to Ti foil, In₂O₃ and NiO separately.

According to the energy level distribution of TiO₂, In₂O₃ and NiO, the proposed interface energies of InNi/N/TiO₂ are illustrated in Fig. 9. As shown in Fig. 9a, the work functions of TiO₂, In₂O₃ and NiO are about 4.2 eV,^{42, 43} 4.4 eV⁴⁴ and 5.3 eV,⁴⁵ respectively according to previous literature. On the InNi/N/TiO₂ photoelectrode, as shown in Fig. 9b, the energy bands of rutile TiO₂ bend upward and In₂O₃ bend downward on the interface of TiO₂ and In₂O₃. The energy bands of In₂O₃ bend upward and NiO bend downward on the In₂O₃ and NiO interface (Fig. 9b). As a result of the band bending, the transfer of photo-induced electrons from TiO₂ to In₂O₃ and NiO is difficult because of the potential barrier between both the interfaces of TiO₂ and In₂O₃ and the In₂O₃ and NiO. The photoinduced electrons have a great tendency to transfer from TiO₂ to Ti foil, and then to the counter electrode. In addition, the band bending could favor the transfer of photo-induced holes from TiO₂ to In₂O₃ and NiO. The analysis above suggests that suitable choice of the metal oxide components could improve the photoelectrochemical properties of TiO₂ photoelectrode by constructing the interfaces that is favorable for the transfer and separation of the photo-induced carriers, which is supported well by the experimental results.

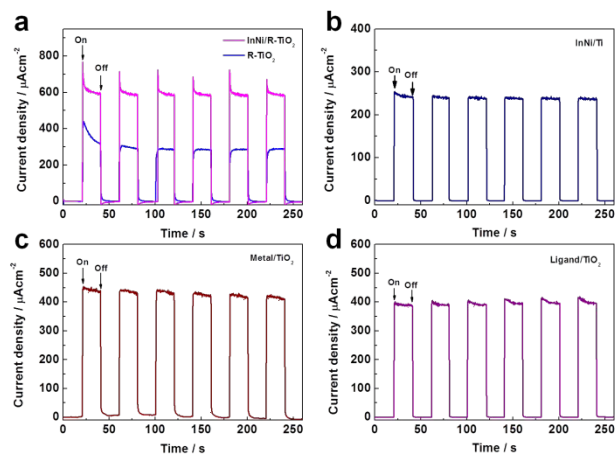


Fig. 10 Transient photocurrents for (a) InNi/R-TiO₂ and R-TiO₂, (b) InNi/Ti, (c) Metal/TiO₂ and (d) Ligand/TiO₂ photoelectrodes at 0.6 V vs SCE under 100 mW/cm² simulated sunlight illumination.

To understand the role of Ti³⁺ doped TiO₂ substrate and the impact of different chemical species in the synthesis solution, we conducted control synthesis experiments by using different substrates and different chemical species in the solvothermal synthesis. As shown in Fig. 10a, if the rutile TiO₂ without Ti³⁺ substrate was used, after the surface modification (called as InNi/R-TiO₂), the performance of the photoelectrode (InNi/R-TiO₂) is twice as high as that of the photoelectrode without surface modification (R-TiO₂). It shows that this modification strategy can also be applied to other types of TiO₂ photoelectrodes. The photocurrent of InNi/R-TiO₂ photoelectrode is 0.6 mA/cm², which is much lower than 1.29 mA/cm² of the InNi/N/TiO₂ photoelectrode. If Ti foil was used as the substrate, the photocurrent of the photoelectrode is about 250 mA/cm², as shown in Fig. 10b. It indicates that the Ti³⁺ doped TiO₂ substrate is crucial for the enhancement of photoelectrochemical activities. With only In and Ni salts in the synthesis (Metal/TiO₂) without the organic ligands or with only ligands (Ligand/TiO₂) without metal precursors in the synthesis solution, the obtained photoelectrodes showed reduced photocurrents as shown in Fig. 10c and d. These could be because the individual organic ligands or metal precursors couldn't form the atomically organized crystalline MOF on the surface of TiO₂. Without MOF precursors, the N doping and In₂O₃ and NiO modification couldn't form on the surface of TiO₂ electrode in one step. The results show the important role of InNi-MOF plays for the improvement of the photoelectrochemical activities.

Moreover, we also investigated the roles of synthesis time, temperatures of the heat treatment to the performance of the obtained photoelectrodes. With longer hydrothermal synthesis time, such as 12 h, the crystals of the InNi-MOF grew into large rods with the size of micrometers on the surface of TiO₂, as shown in Fig. S2a. After heat treatment at 600 °C, the morphology of the rods remains as shown in the Fig. S2b and c. The photoelectrochemical reactivity of the sample treated for 12 h is much lower than that of samples treated for 6 h (Fig. S3). This could be because the longer synthesis

time resulted in large sized In₂O₃ and NiO, which is disadvantage for the homogeneous distribution of metal oxides on the surface of TiO₂. A suitable size of the metal oxides controlled by the growth conditions of the MOF precursor is a key factor for the improved activity of the photoelectrode. Fig. S4 shows the photocurrent tested from InNi/N/TiO₂ photoelectrode annealed at different temperatures (400 °C, 500 °C, 600 °C, 700 °C), which indicated that the 600 °C is the best temperature for the heat treatment.

Experimental

Synthesis of TiO₂ photoelectrode

The TiO₂ photoelectrode was synthesized based on the previous work.⁶ A 1×2 cm Ti foil (0.25 mm thickness, 99.5 % trace metal, Alfa Aesar) was cleaned by sonication in ethanol, acetone, isopropanol and deionized water separately. Then the clean Ti foil was placed in a teflon-lined stainless steel autoclave which contained 10 mL aqueous HCl solution (0.45 M), and treated at 220 °C for 12 h. After reaction, the product was collected and washed with deionized water several times. A blue film was grown on the surface of the Ti foil. The TiO₂ photoelectrode prepared from the above procedures was placed in a teflon-lined stainless steel autoclave containing 10 mL aqueous N₂H₄ solution (20 % by weight). The autoclave was heated at 220 °C for 20 h. Then, the product was collected and washed with deionized water several times.

Synthesis of modified TiO₂ photoelectrodes

33.4 mg indium chloride (InCl₃), 24.4 mg nickel (II) chloride hexahydrate (NiCl₂•6H₂O), 26 mg terephthalic acid (C₈H₆O₄) and 10 mg 1,2,4-triazole (C₂H₃N₃) were added into a 20 mL glass vial containing a mixed solvent of 4 g N,N-Dimethylmethanamide (C₃H₇NO) and 0.8 g deionized water. After stirring for 30 min, the TiO₂ photoelectrode was immersed into the solution for 30 min. Then, the vial was sealed and treated at 120 °C for 6 h. After reaction, the TiO₂ electrode was collected and washed with deionized water and ethanol for several times. Then, the samples were dried by Ar flow. At last, the photoelectrode was treated in a furnace at 600 °C with N₂ flow for 2 h.

Characterization

X-ray diffraction (XRD) patterns of the samples were recorded on Bruker D8 powder diffractometer using Cu irradiation. Morphologies and structures of the prepared samples were further examined with a Philips Nova NanoSEM450 scanning electron microscope (SEM). Transmission electron microscope (TEM) and High-resolution Transmission electron microscope (HRTEM) images were obtained with a JEM 2010F field emission gun transmission electron microscope operated at an accelerating voltage of 200 kV. Chemical compositions and states of the TiO₂ samples were analyzed using X-ray photoelectron spectroscopy (XPS, Thermo Escalab 250Xi, a monochromatic Al K_α X-ray source). All binding energies were referenced to the C 1s peak (284.8 eV) arising from adventitious

carbon. The optical absorbance spectra of the samples were recorded in a shimadzu UV-3101PC UV-Vis-NIR spectrophotometer.

Photoelectrochemical measurement

Photoelectrochemical performance was investigated using solartron 1287 Electrochemical Workstation in a standard three-electrode cell with the TiO₂-based working electrode, a Pt foil counter electrode, and a saturated calomel reference electrode, respectively. The light source was a 150 W Xenon lamp (Newport, 69907) coupled with an AM 1.5G filter (Newport, 81094). Light intensity was adjusted to 100 mW/cm² with a radiant power meter (Newport, 70260) combined with a probe (Newport, 70268). 0.5 M Na₂SO₄ (pH=6.3) purged with Ar was used as the electrolyte. In addition, Xenon lamp with a filter (Newport, FR-GG400) was used to produce a visible light source below the wavelength of 400 nm. The incident photon to current efficiency (IPCE) was measured under the same xenon lamp equipped with a monochromator (Newport, 74404).

Conclusions

The conclusions we developed a simple one pot synthetic method that can combine the heteroatom doping strategy with surface modification of metal oxides on TiO₂ photoelectrode. The In₂O₃ and NiO modified rutile TiO₂ electrode with co-doping of N and Ti³⁺ was obtained here. The co-doping of N and Ti³⁺ to TiO₂ extended the absorption edge and enhanced the light absorption of TiO₂ in the visible region and increased the donor density. At the same time, the surface modification by In₂O₃ and NiO also passivated the surface trap states and constructed the appropriate interfaces for promoting the separation and transfer of photogenerated charges. Subsequently, the modified TiO₂ photoelectrode showed superior photoelectrochemical performance under both simulated sunlight (2.7 times) and visible light (near 2 times) illumination compared to the pristine TiO₂ photoelectrode. Suitable substrate of the electrode, appropriate size of MOF precursor and choice of ligands with metal ions all play important roles in improving the performance of the materials. The modification method shown here could potentially serve as a new promising way in the fabrication of high-performance PEC device for both TiO₂ and other types of semiconductors.

Conflicts of interest

There are no conflicts to declare.

Acknowledgements

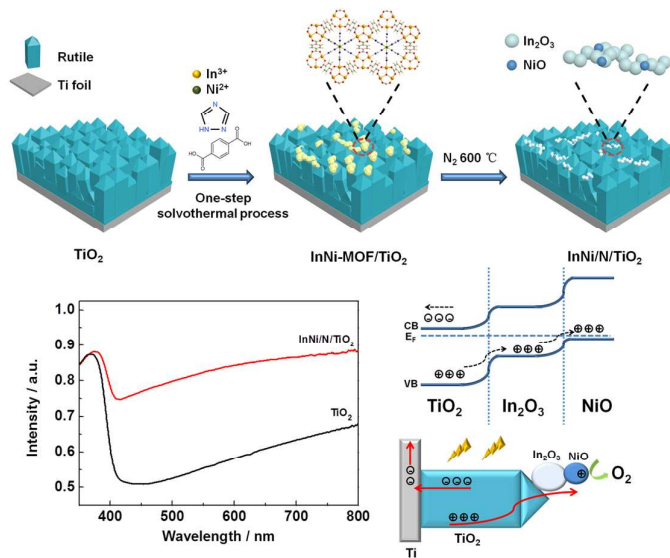
The research is mainly supported by US Department of Energy, Office of Basic Energy Sciences, Materials Sciences and Engineering Division under Award No. DE-SC0010596 (P.F) (on the synthesis of MOF and electrochemical characterization). Dr. Wei Jiao thanks for the financial support of the NSFC (51402314) and China Postdoctoral Science Foundation (2016M601501) (on

the SEM and XPS characterizations). The authors also thank Dr. Yangtao Zhou for his help in TEM characterization.

References

1. N. S. Lewis, *Science*, 2007, **315**, 798-801.
2. A. Landman, H. Dotan, G. E. Shter, M. Wullenkord, A. Houaijia, A. Maljusch, G. S. Grader and A. Rothschild, *Nat Mater*, 2017, **16**, 646-651.
3. A. Fujishima and K. Honda, *Nature*, 1972, **238**, 37-38.
4. W. Jiao, Y. Xie, R. Chen, C. Zhen, G. Liu, X. Ma and H.-M. Cheng, *Chem. Commun.*, 2013, **49**, 11770-11772.
5. F. Ning, M. Shao, S. Xu, Y. Fu, R. Zhang, M. Wei, D. G. Evans and X. Duan, *Energy. Environ. Sci.*, 2016, **9**, 2633-2643.
6. C. Mao, F. Zuo, Y. Hou, X. Bu and P. Feng, *Angew. Chem. Int. Ed.*, 2014, **53**, 10485-10489.
7. T. M. R. Asahi, T. Ohwaki, K. Aoki, Y. Taga, *Science*, 2001, **293**, 269-271.
8. G. Liu, H. G. Yang, X. W. Wang, L. N. Cheng, J. Pan, G. Q. Lu and H. M. Cheng, *J. Am. Chem. Soc.*, 2009, **131**, 12868-12869.
9. G. Liu, L. C. Yin, J. Q. Wang, P. Niu, C. Zhen, Y. P. Xie and H. M. Cheng, *Energy. Environ. Sci.*, 2012, **5**, 9603.
10. R. Negishi, S.-i. Naya, H. Kobayashi and H. Tada, *Angew. Chem. Int. Ed.*, 2017, **56**, 10347-10351.
11. M. D. Ye, J. J. Gong, Y. K. Lai, C. J. Lin and Z. Q. Lin, *J. Am. Chem. Soc.*, 2012, **134**, 15720-15723.
12. W. N. Wang, W. J. An, B. Ramalingam, S. Mukherjee, D. M. Niedzwiedzki, S. Gangopadhyay and P. Biswas, *J. Am. Chem. Soc.*, 2012, **134**, 11276-11281.
13. W. X. Ouyang, F. Teng and X. S. Fang, *Adv. Funct. Mater.*, 2018, **28**, 1707178.
14. H. G. Yang, C. H. Sun, S. Z. Qiao, J. Zou, G. Liu, S. C. Smith, H. M. Cheng and G. Q. Lu, *Nature*, 2008, **453**, 638-641.
15. S. W. Liu, J. G. Yu and M. Jaroniec, *J. Am. Chem. Soc.*, 2010, **132**, 11914-11916.
16. C. W. Kim, S. J. Yeob, H.-M. Cheng and Y. S. Kang, *Energy. Environ. Sci.*, 2015, **8**, 3646-3653.
17. G. Wang, H. Wang, Y. Ling, Y. Tang, X. Yang, R. C. Fitzmorris, C. Wang, J. Z. Zhang and Y. Li, *Nano. Lett.*, 2011, **11**, 3026-3033.
18. S. Hoang, S. Guo, N. T. Hahn, A. J. Bard and C. B. Mullins, *Nano. Lett.*, 2012, **12**, 26-32.
19. M. Y. Wang, L. Sun, Z. Q. Lin, J. H. Cai, K. P. Xie and C. J. Lin, *Energy. Environ. Sci.*, 2013, **6**, 1211-1220.
20. M. Zhao, K. Yuan, Y. Wang, G. Li, J. Guo, L. Gu, W. Hu, H. Zhao and Z. Tang, *Nature*, 2016, **539**, 76-80.
21. X. Cao, C. Tan, M. Sindoro and H. Zhang, *Chem. Soc. Rev.*, 2017, **46**, 2660-2677.
22. X. Zhao, X. Bu, E. T. Nguyen, Q.-G. Zhai, C. Mao and P. Feng, *J. Am. Chem. Soc.*, 2016, **138**, 15102-15105.
23. W. Jiao, Y. P. Xie, R. Z. Chen, C. Zhen, G. Liu, X. L. Ma and H. M. Cheng, *Chem. Commun.*, 2013, **49**, 11770-11772.
24. A. N. Mansour, *Surface Science Spectra*, 1994, **3**, 231-238.
25. G. Ertl, R. Hierl, H. Knözinger, N. Thiele and H. P. Urbach, *Appl. Surf. Sci.*, 1980, **5**, 49-64.
26. J. Gan, X. Lu, J. Wu, S. Xie, T. Zhai, M. Yu, Z. Zhang, Y. Mao, S. C. I. Wang, Y. Shen and Y. Tong, *Sci Rep-Uk*, 2013, **3**, 1021.
27. W. Jiao, N. Li, L. Wang, L. Wen, F. Li, G. Liu and H. M. Cheng, *Chem. Commun.*, 2013, **49**, 3461-3463.
28. R. Asahi, T. Morikawa, T. Ohwaki, K. Aoki and Y. Taga, *Science*, 2001, **293**, 269-271.
29. J. Mu, B. Chen, M. Zhang, Z. Guo, P. Zhang, Z. Zhang, Y. Sun, C. Shao and Y. Liu, *ACS. Appl. Mater. Inter.*, 2012, **4**, 424-430.

30. T. Sreethawong, Y. Suzuki and S. Yoshikawa, *Int. J. Hydrogen. Energ.*, 2005, **30**, 1053-1062.
31. G. Liu, H. G. Yang, X. Wang, L. Cheng, H. Lu, L. Wang, G. Q. Lu and H.-M. Cheng, *The Journal of Physical Chemistry C*, 2009, **113**, 21784-21788.
32. O. Neufeld, N. Yatom and M. Caspary Toroker, *Acs Catal.*, 2015, **5**, 7237-7243.
33. F. Le Formal, N. Tetreault, M. Cornuz, T. Moehl, M. Gratzel and K. Sivula, *Chem Sci*, 2011, **2**, 737-743.
34. S. A. Ali Yahia, L. Hamadou, A. Kadri, N. Benbrahim and E. M. M. Sutter, *J. Electrochem. Soc.*, 2012, **159**, K83-K92.
35. G. Wang, Y. Yang, D. Han and Y. Li, *Nano Today*, 2017, **13**, 23-39.
36. X. Song, W. Li, D. He, H. Wu, Z. Ke, C. Jiang, G. Wang and X. Xiao, *Adv. Energy. Mater.*, 2018, **8**, 1800165.
37. H. I. Kim, D. Monllor-Satoca, W. Kim and W. Choi, *Energy. Environ. Sci.*, 2015, **8**, 247-257.
38. A. Renaud, L. Cario, Y. Pellegrin, E. Blart, M. Boujtita, F. Odobel and S. Jobic, *Rsc Adv*, 2015, **5**, 60148-60151.
39. C. Zhen, L. Wang, L. Liu, G. Q. Lu and H.-M. Cheng, *Chem. Commun.*, 2013, **49**, 6191-6193.
40. Y.-S. Hu, A. Kleiman-Shwarscstein, G. D. Stucky and E. W. McFarland, *Chem. Commun.*, 2009, **0**, 2652-2654.
41. Z. Zhang, M. N. Hedhili, H. Zhu and P. Wang, *Phys. Chem. Chem. Phys.*, 2013, **15**, 15637-15644.
42. A. Arango, S. Carter, P. Brock, *Appl. Phys. Lett.* 1999, **74**, 1698-1700.
43. A. Imanishi, E. Tsuji, Y. Nakato, *The Journal of Physical Chemistry C* 2007, **111**, 2128-2132.
44. A. Klein, *Appl. Phys. Lett.* 2000, **77**, 2009-2011.
45. M. D. Irwin, J. D. Servaites, D. B. Buchholz, B. J. Leever, J. Liu, J. D. Emery, M. Zhang, J.-H. Song, M. F. Durstock, A. J. Freeman, M. J. Bedzyk, M. C. Hersam, R. P. H. Chang, M. A. Ratner, T. J. Marks, *Chem. Mater.* 2011, **23**, 2218-2226.



In_2O_3 and NiO modified rutile TiO_2 electrode with co-doping of N and Ti^{3+}